Volume 55
Number 11
17 March 2026
Pages 4345-4750

rticle Online
Issue

Dalton Transactions

An international journal of inorganic chemistry

rsc.li/dalton

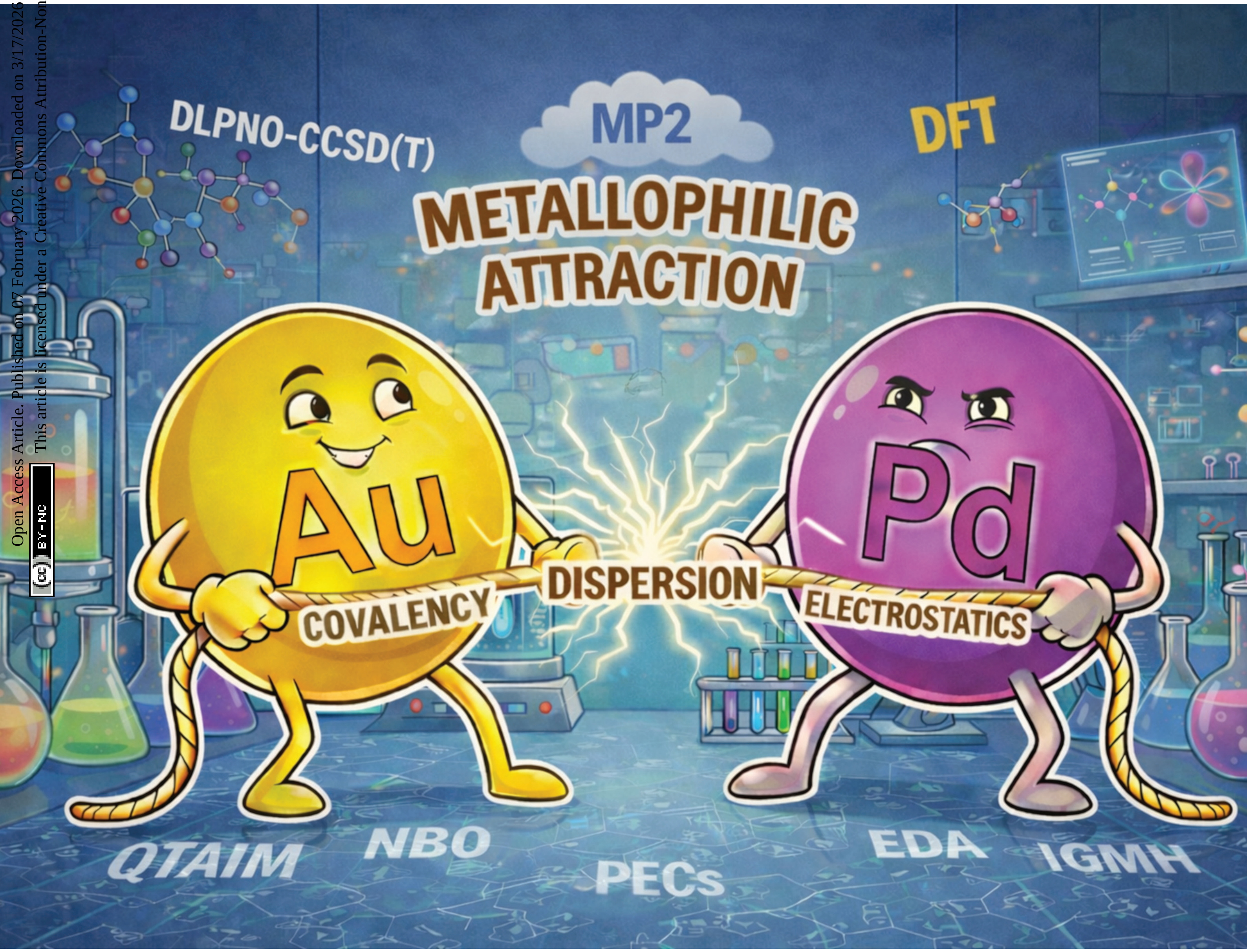

ISSN 1477-9226

ROYAL SOCIETY OF CHEMISTRY

PAPER

José M. López-de-Luzuriaga, Miguel Monge *et al.*

On the nature and feasibility of unsupported Au···Pd metallophilic interactions: a correlated computational study

View Article Online

Dalton Transactions

PAPER

Cite this: *Dalton Trans.*, 2026, **55**, 4406

On the nature and feasibility of unsupported Au⋯Pd metallophilic interactions: a correlated computational study

Félix Reboiro, M. Elena Olmos, José M. López-de-Luzuriaga * and Miguel Monge *

Received 5th January 2026,
Accepted 2nd February 2026

DOI: 10.1039/d6dt00023a

rsc.li/dalton

Unsupported Au⋯Pd interactions have not yet been experimentally confirmed, leaving their existence and fundamental nature an open question. Herein, we present a comprehensive multifaceted computational study to grasp their nature and feasibility, using simplified models of typical Au(I)/Au(III) and Pd(II) complexes. Geometry optimizations and interaction energy calculations were carried out at both the DFT and post-Hartree–Fock levels of theory, including MP2, SCS-MP2 and DLPNO-CCSD(T) methods. Potential energy curves computed at the MP2 and RHF levels of theory with different relativistic ECPs allowed us to disentangle the effects of electron correlation and relativistic contributions. In-depth topological analyses based on MP2 and DLPNO-CCSD(T) electron densities were conducted to gain deeper insight into the bonding character. Additionally, we also propose a decomposition scheme to isolate the metal–metal contribution to the total interaction energy; a term whose true nature, repulsive or attractive, remains debatable. This computational protocol, together with the reduced size of the simplified models, provides a consistent and reliable framework for the high-accuracy characterization of metallophilic interactions. Remarkably, the computed Au⋯Pd interaction energy values are stronger than anticipated (10–35 kJ mol^{-1}), with a predominantly ionic and dispersive, closed-shell character and a minor covalent contribution. In these systems, medium-to-strong metal–hydrogen interactions are also present, coexisting and competing with the metallophilic contacts to influence the overall stabilization. Collectively, our results point to the potential existence of related compounds featuring unsupported Au⋯Pd contacts in suitably designed systems, where substantial electrostatic forces further stabilize the models.

1. Introduction

Simple well-known electrostatics would predict repulsion between closed- or pseudo closed-shell metal cations,[1] yet experimental studies have shown that these species can indeed attract each other,[2–4] forming discrete complexes,[5] chains,[6] or 2- and 3-dimensional networks.[7] First identified in gold(I) compounds as aurophilicity,[8] this phenomenon, now broadly recognized as metallophilicity,[9] represents a class of weak yet highly directional interactions that play a key role in structural organization. Typically described as van der Waals-type forces (20–50 kJ mol^{-1}),[10] they arise from dispersion-type effects and are reinforced by the pronounced relativistic contributions in heavy atoms.[11–13] Despite extensive investigation,[14–20] the precise physical origin and underlying nature of metallophilic interactions remain under debate.[21]

Experimental and computational studies have revealed numerous metallophilic contacts across a variety of metal cation types, including d^{10} species Au(I), Ag(I), Cu(I), and Hg(II),[22–27] d^{8} species Au(III), Pd(II), and Pt(II),[28–32] and d^{10}s^{2} species Tl(I), Ge(II), Pb(II), and Bi(III).[33–36] These interactions are observed in both homometallic and heterometallic complexes, where they can coexist with or compete against other recurring noncovalent motifs, such as metal–hydrogen or metal–halogen bonding.[37–41] Depending on the system, this competitive–cooperative balance determines whether metallophilicity acts as an auxiliary interaction or emerges as the dominant one controlling the overall structural arrangement. Notably, metallophilic interactions are predominantly observed in the solid state, as their intrinsic weakness often prevents them from persisting in solution.[10]

These subtle yet powerful noncovalent interactions, particularly those involving Au(I) cations, are far from being mere spectators. They not only orchestrate supramolecular assemblies[42–44] but also stabilize reactive intermediates in catalysis,[45–47] enable sensing applications,[48,49] and drive intriguing phenomena such as mechanochromism,[50,51] vapochro-

---

Departamento de Química, Instituto de Investigación en Química de la Universidad de La Rioja (IQUR), Madre de Dios 53, 26006 Logroño, La Rioja, Spain. E-mail: josemaria.lopez@unirioja.es, miguel.monge@unirioja.es

mism,[52] and luminescence,[53] making them key contributors in functional materials, including OLED technology.[54]

Focusing on gold–palladium heterometallic complexes, the first one reported to feature a supported Au(I)⋯Pd(II) interaction, [{AuCl(Ph_2PCH_2SPh)}$_2$$PdCl_2$] (complex **1**, Scheme 1A), was synthesized in 2000 by Crespo and co-workers.[55] X-ray diffraction studies revealed a trinuclear arrangement with an Au–Pd distance of 3.1418(8) Å, where the interaction is not sterically enforced owing to the flexibility and length of the bridging ligand. Complementary LMP2 calculations reveal that the Au(I)⋯Pd(II) interaction reaches ∼35 kJ mol^{-1} and is governed primarily by dispersion, with only a minor ionic contribution. The comparable energetic contributions of Pd → Au and Au → Pd donation result in negligible net charge transfer.

Later, Xia *et al.* synthesized the complexes [Pd(CN)$_2$(μ-dcpm)$_2$Au]X, where dcpm is bis(dicyclohexylphosphino) methane and X represents Cl^- or ClO_4^- counterions (complexes **2** and **3**, Scheme 1A).[56] The X-ray crystal structure of complex **2** showed that the bridging diphosphine ligand brings the metal centers closer, resulting in an Au–Pd distance of 2.954(1) Å, shorter than the sum of their van der Waals radii.[57–59] This complex exhibits photoluminescence properties with an emission at 510–520 nm and lifetimes in the microsecond range.

More recently, Wächtler and co-workers reported a family of d^{10}–d^8 heterobimetallic species, including the Au–Pd complex [Pd(PMe_3)$_2$(μ-2-$C_6F_4PPh_2$)$_2$Au]PF_6 (complex **4**, Scheme 1A),[60] whose X-ray crystal structure revealed an Au–Pd distance of 2.7970(4) Å, while NCI and ELF analyses indicated an attractive noncovalent interaction predominantly governed by dispersion forces, consistent with a metallophilic contact. In addition, a recent computational investigation of unsupported Au(I)/Ag(I) ⋯Pd(II) model systems provided a novel covalent perspective for understanding and visualizing these closed-shell interactions.[61]

As illustrated by the preceding examples, supported Au⋯Pd interactions are now well established in heterometallic chemistry; however, genuine unsupported Au⋯Pd contacts have not yet been reported. This stands in contrast to the abundance of Au(I)⋯Au(I) and Pd(II)⋯Pd(II) motifs commonly found in homometallic systems.[22,29,30] In addition, gold-containing heterometallic complexes have attracted considerable attention as highly tunable platforms to explore novel properties and applications.[62–66] Beyond structural interest, these complexes provide valuable insights into the debated nature of metallophilic interactions and may exhibit unique properties or functionalities, making their design and synthesis particularly appealing.

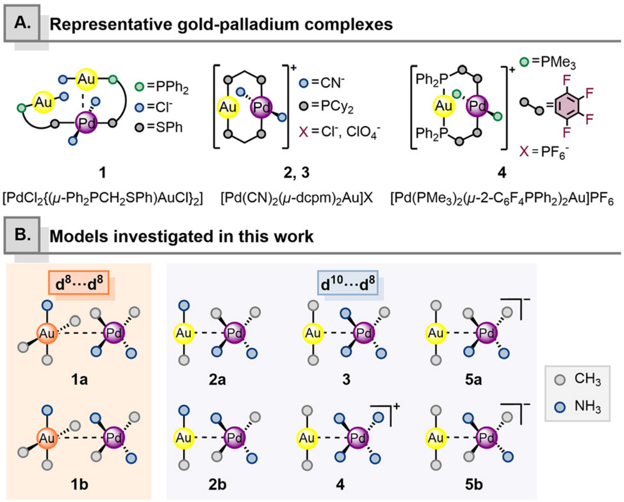

Scheme 1 (A) Representative gold–palladium complexes in the literature. (B) Computational models studied in the present work.

Our recent computational efforts have focused on the nature of unsupported Au⋯M(d^8) metallophilic interactions.[67–69] We have demonstrated that Au(I)/Au(III)⋯Pt(II) contacts are viable, with MP2 calculations on neutral and cationic models yielding interaction energy values between 10 and 45 kJ mol^{-1}. While these interactions are mainly ionic and dispersive with minor covalency, their overall stability is significantly bolstered by metal–hydrogen bonding. In many instances, these secondary ligand-based contacts contribute as much to the total stabilization as the direct metallophilic interaction itself.

Herein, we extend this work to neutral and ionic Au(III)/Au(I)–Pd(II) systems (see Scheme 1B). Using a robust computational protocol with high-level correlated wave function methods, we characterized and isolated the metal–metal contribution to the total interaction energy. This study not only deciphers the intrinsic nature and strength of these contacts but also identifies the most feasible candidates for experimental synthesis, offering a strategic framework for the rational design of future heterometallic complexes.

2. Computational methods

Gas-phase optimization of all computational models was performed without any geometrical constraints using the Gaussian 16 program package.[70] A range of computational methods was systematically employed, including the RHF[71] and MP2 levels of theory,[72,73] as well as a DFT approach[74,75] within PBE0-D3BJ,[76,77] M06-L,[78] and M06-2X functionals.[79] The Karlsruhe def2-TZVP basis sets were employed throughout,[80] in combination with 60-electron and 28-electron effective core potentials (def2-ECPs) for Au and Pd atoms,[81] respectively. Additional post-HF optimizations were performed at the SCS-MP2 level of theory,[82] considering both ZORA all-electron (ZORA-TZVP)[83] and def2-ECPs basis sets (def2-TZVP). These calculations were performed with ORCA 6 software,[84] employing the RIJCOSX approximation[85] along with auxiliary basis sets. Frequency calculations confirmed that all optimized geometries correspond to true minima.

Interaction energy (ΔE_{int}) values were corrected using the counterpoise method (eqn (S1)) to account for basis set superposition error (BSSE) at the same level of theory employed for the optimizations.[86] Potential energy curves (PECs) were generated by varying the Au–Pd distance and ΔE_{int} values were fitted using the four-parameter Herschbach–Laurie function (eqn (S2)).[87] To investigate the relativistic effects, fully relativistic (ECP-MDF) and non-relativistic (ECP-MHF) effective core potentials were applied to evaluate the interaction energies along the PECs.[88–90] Finally, the ΔE_{int} values at the minimum of the PECs were further refined at the RHF, MP2, SCS-MP2, and DLPNO-CCSD(T)[91] levels of theory using def2-TZVP basis sets. Moreover, the metal–metal (M–M) component of the overall interaction energy was evaluated following the protocol outlined in Scheme S1.

Electronic structure analyses included the natural bond orbital (NBO),[92] and Wiberg bond orders (WBOs)[93] were calculated at the MP2/def2TZVP level of theory. In addition, intrinsic bond strength indices (IBSIs)[94] and fuzzy bond orders (FBOs)[95] were computed at the MP2 and DLPNO-CCSD(T)/def2-TZVP levels of theory employing Multiwfn 3.8 software.[96]

The total interaction energy of each model was partitioned using energy decomposition analysis coupled with natural orbital for chemical valence (EDA-NOCV)[97,98] at the DLPNO-MP2/def2-TZVP level of theory using the ORCA 6 package.[99] A complementary decomposition, distinguishing dispersive and non-dispersive contributions, was performed *via* local energy decomposition (LED),[100] within the DLPNO-CCSD(T) framework as implemented in the ORCA 6 program.

Finally, topological analyses of the MP2/def2-TZVP and DLPNO-CCSD(T)/def2-TZVP electron densities were performed using the quantum theory of atoms in molecules (QTAIM)[101] and the independent gradient model based on Hirshfeld partition (IGMH),[102] as implemented in Multiwfn software. The resulting representations were generated and visualized using the VMD 1.9.4a software package.[103] In addition, comprehensive computational details, including theoretical background and equations, are provided in the SI.

3. Results and discussion

3.1 Computational models and optimizations

Computational models were designed to simulate prototypical linear gold(I) and orthometallated gold(III)/palladium(II) complexes,[104–106] in which the original donor groups were replaced with methyl and ammonia ligands (more details are included in the SI). This approach enables a clear and focused investigation of Au⋯Pd interactions while preserving chemical relevance. The use of simplified models effectively describes the fundamental features of experimental systems, allowing the computational insights to be directly extrapolated to real-world chemical environments. Following this strategy,[67–69] we constructed simplified neutral, cationic, and anionic unsupported models to systematically explore the nature, strength and feasibility of the targeted metallophilic interactions.

Hence, neutral models *cis*-/*trans*-$[Pd(CH_3)_2(NH_3)_2][Au(CH_3)_3(NH_3)]$ (models **1a**/**1b**) were built to investigate Pd(II)⋯Au(III) interactions, whereas *cis*-/*trans*-$[Pd(CH_3)_2(NH_3)_2][Au(CH_3)(NH_3)]$ (models **2a**/**2b**) and $[Pd(CH_3)(NH_3)_3][Au(CH_3)_2]$ (model **3**) were designed to study Pd(II)⋯Au(I) interactions in neutral complexes. To extend this analysis to charged complexes, $\{[Pd(NH_3)_4][Au(CH_3)_2]\}^+$ (model **4**) and *cis*-/*trans*-$\{[Pd(CH_3)_2(NH_3)_2][Au(CH_3)_2]\}^-$ (models **5a** and **5b**) were developed for cationic and anionic complexes, respectively (see Scheme 1B). In principle, these geometries are well-suited to facilitate the formation of Au⋯Pd metallophilic interactions.

Initially, all structures were fully optimized at the MP2/def2-TZVP level of theory without any geometric constraints. We selected the MP2 level of theory because it provides reliable geometries for small molecular complexes in which dispersion plays a key role,[107] and it has proved to be a dependable level of theory for studying metallophilic interactions.[11–13] The resulting optimized geometries are shown in Fig. 1, and selected bond lengths and angles are listed in Table S1.

Most structures display Au⋯Pd contacts ranging from 2.91 to 3.45 Å, which are shorter than the sum of their van der Waals radii (*i.e.* 4.25 Å or 4.47 Å, depending on the reference).[58,59] The linear and square-planar geometries of the Au(I) and Au(III)/Pd(II) fragments, respectively, facilitate metal–metal interactions by positioning the metal centers in nearly parallel planes. Additionally, Au(I)–Pd(II) distances are generally shorter than the Au(III)–Pd(II) ones. This trend is expected, as Au(III) is more electron-deficient (*i.e.*, more Lewis acid character), leading to greater depletion of electron density. This behavior is fully consistent with the NBO metal charges and, in principle, makes Au(III) less suited to engage in stronger metallophilic interactions. In addition, its square-planar geometry increases steric hindrance between ligands, while relativistic effects are less pronounced than in Au(I) cations, further reducing the metal–metal interaction.[108]

Furthermore, all models display additional noncovalent interactions, most commonly metal–hydrogen contacts, that contribute to the stabilization of the dyad. Notably, in models **2b** and **5a**, these secondary interactions dominate, effectively masking the metallophilic contacts. Thus, they can either support or compete with metal–metal interactions in stabilizing the overall structure.

The same set of structures was also optimized at the RHF/def2-TZVP level of theory without any geometric constraints, with the resulting geometries displayed in Fig. 2 and key bond parameters listed in Table S1.

The RHF-optimized structures remain broadly similar to their MP2 counterparts, except for **2b**, which undergoes a pronounced distortion. Two clear trends emerge from a comparison of the optimized geometries: (i) the Au–Pd distances increase markedly (≈0.5–0.8 Å), indicating a substantial weakening of the metal–metal interaction. This underscores the crucial role of electron correlation effects (*i.e.*, dispersion) in stabilizing these contacts. Notably, the cationic model **4**, in which electrostatic forces dominate, exhibits only a modest Au–Pd elongation (≈0.2 Å) relative to the other complexes. (ii) Secondary noncovalent interactions, mainly metal–H contacts, are likewise weakened at the RHF level of theory, but much less so than the Au⋯Pd interactions, reflecting their more ionic character.

Consistent with these observations, NBO metal charges increase relative to MP2 values, indicating electron density

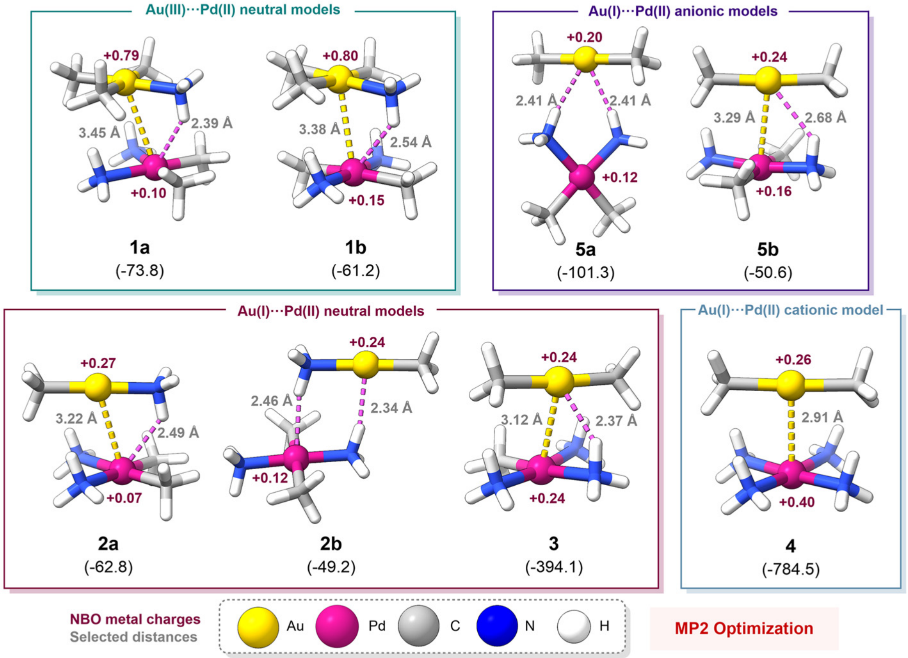

Fig. 1 Representations of the MP2/def2-TZVP optimized structures of models **1–5**. Key interatomic distances, NBO metal charges, and interaction energy values reported in kJ mol^{-1} (in parentheses) computed at the same level of theory are displayed.

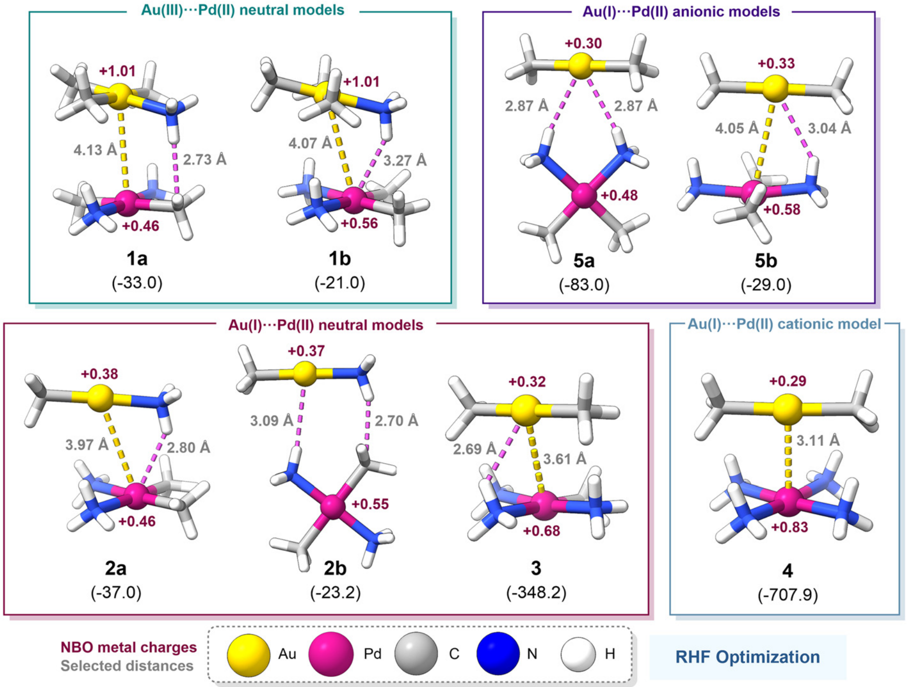

Fig. 2 Representations of the RHF/def2-TZVP optimized structures of models **1–5**. Key interatomic distances, NBO metal charges, and interaction energy values reported in kJ mol^{-1} (in parentheses) computed at the same level of theory are displayed.

depletion at both metal centers, and the interaction energy values also decrease systematically, further evidencing the overall weakening of the interactions. Together, these trends reinforce the well-established principle that dispersion effects are essential for accurately describing noncovalent interactions, particularly metallophilic ones.[1,11–13]

In addition, these geometries were re-optimized at the higher-level SCS-MP2 method to more rigorously account for electron correlation effects and thereby benchmark the MP2/def2-TZVP optimized structures. Calculations were carried out using both def2-TZVP and all-electron ZORA-TZVP basis sets (see Table S1, SI). The resulting structures are consistent with those obtained at the MP2 level of theory, showing a systematic elongation of the M–M distance, which becomes more pronounced when scalar relativistic effects are included *via* the ZORA formalism. This behavior is consistent with the well-known tendency of the MP2 level of theory to overestimate metal–metal attraction, while still providing a reliable qualitative description.[109] To further validate these results, several DFT functionals were assessed (see Table S2). The optimized structures also show good agreement with the correlated methods, with PBE0-D3(BJ) offering the closest correspondence to the SCS-MP2-ZORA geometries. In line with these structural trends, the interaction energy values obtained at their respective levels of theory (see Table S3) display patterns comparable to those observed at the MP2 level of theory.

Finally, representative models were re-optimized using a polar implicit solvent, such as tetrahydrofuran (THF), to assess whether the metallophilic interaction persists in solution. The results show a weakening of the interaction energy, while the overall geometries remain essentially unchanged, with the Au⋯Pd interaction still prevailing (see Fig. S1).

Taken together, the benchmarked structures that preserve metallophilic contacts (see Fig. 1), namely all models except **2b** and **5a**, suggest potentially attractive Au⋯Pd interactions. Although metal–metal distances alone cannot unambiguously establish metallophilic contacts,[110] these models still provide reliable platforms for the computational and topological exploration of Au⋯Pd interactions (*vide infra*).

3.2 Potential energy curves

As a next step, potential energy curves (PECs) were computed based on the MP2-optimized structures to identify the Au–Pd distance at which the interaction reaches its minimum. Counterpoise-corrected interaction energies were evaluated at the RHF and MP2/def2-TZVP levels of theory using quasi-relativistic (QR), fully relativistic (FR), and nonrelativistic (NR) ECPs for the metal centers. The resulting PECs are shown in Fig. 3, and additional computational details are provided in the SI.

Analysis of the PECs offers clear insights into the strength and nature of the interactions. As the two metal centers approach, the interaction energy decreases (more negative, *i.e.*, more attractive), reaching a minimum at the optimal balance between attraction and repulsion. Beyond this point, the interaction weakens as the metals move apart or become repulsive if they are pushed too close. The shape of the curves further illustrates this behavior: a well-defined minimum exhibits attraction, while the absence of a minimum indicates repulsion between the model fragments. Moreover, the role of electron correlation effects, and ultimately dispersion, can be inferred by comparing PECs obtained with methods that treat electron correlation to different extents. To this end, we selected the MP2 method, which inherently captures electron correlation *via* a second-order perturbative treatment, and the RHF level of theory, which neglects it entirely, allowing us to assess the crucial role of electron correlation in accurately describing noncovalent interactions.

That said, two key points should be kept in mind: (i) the PECs capture all interactions in the models, not just the metallophilic ones; (ii) although all dispersion interactions originate from electron correlation effects, not all electron correlation effects account for dispersion,[12] a distinction that is crucial for the discussion that follows.

The calculated PECs for all models confirm the attractive nature of the interactions, as evidenced by well-defined minima at both levels of theory. The RHF-PECs minima highlight the significant role of ionic contributions, while the extra stabilization observed in the MP2-PECs underscores the critical impact of electron correlation effects.

For neutral Au(III)⋯Pd(II) models **1a** and **1b**, the Au–Pd equilibrium distances at the MP2 level of theory are approximately 3.50 Å, with corresponding interaction energy values ranging from −60 to −75 kJ mol^{-1}. It should be noted that the larger number of ligands in these models may contribute to additional stabilization through ligand–ligand interactions.

In contrast, neutral Au(I)⋯Pd(II) models **2a** and **3** display different behaviors. Model **2a** follows the pattern of the previous neutral systems, with an equilibrium distance of approximately 3.40 Å and interaction energy values of −65 kJ mol^{-1}; however, model **3** shows a shorter equilibrium distance of around 3.25 Å and a much stronger interaction energy of −390 kJ mol^{-1}. These pronounced differences in model **3** are attributed to the ionic character of the fragments—$[Au(CH_3)_2]^-\cdots[Pd(CH_3)(NH_3)_3]^+$—which further reinforces the overall interaction *via* strong coulombic forces.

Similarly, the cationic Au(I)⋯Pd(II) model **4** displays the shortest equilibrium distance, approximately 3.00 Å, and the largest interaction energy, −785 kJ mol^{-1}, due to the highly ionic interaction between fragments—$[Au(CH_3)_2]^-\cdots[Pd(NH_3)_4]^{2+}$—and the additional stabilization from the overall positive charge.

Finally, the anionic Au(I)⋯Pd(II) model **5b** exhibits values like model **2a**, with an equilibrium distance of approximately 3.40 Å and an interaction energy of −50 kJ mol^{-1}, indicating that the overall interaction is weaker than in the cationic systems. This may be attributed to the fact that model **5b** is composed of the fragments—$[Au(CH_3)_2]^-\cdots[Pd(CH_3)_2(NH_3)_2]$—which are anionic and neutral, respectively, and therefore exhibit a much lower ionic complementarity than models **3** and **4**. It should be noted that while this local coulombic attraction is significant in the present discrete models, in extended systems, such as crystal structures, the total electrostatic stabilization arises from complex collective summations. These many-body contributions may influence the overall stability beyond the pairwise interactions discussed here.

Comparison of the PECs at the MP2 and RHF levels of theory clearly highlights the importance of electron correlation effects. For the RHF level of theory, all PECs show longer equilibrium distances at the minimum and smaller interaction energy values, reflecting the usual electron correlation-induced

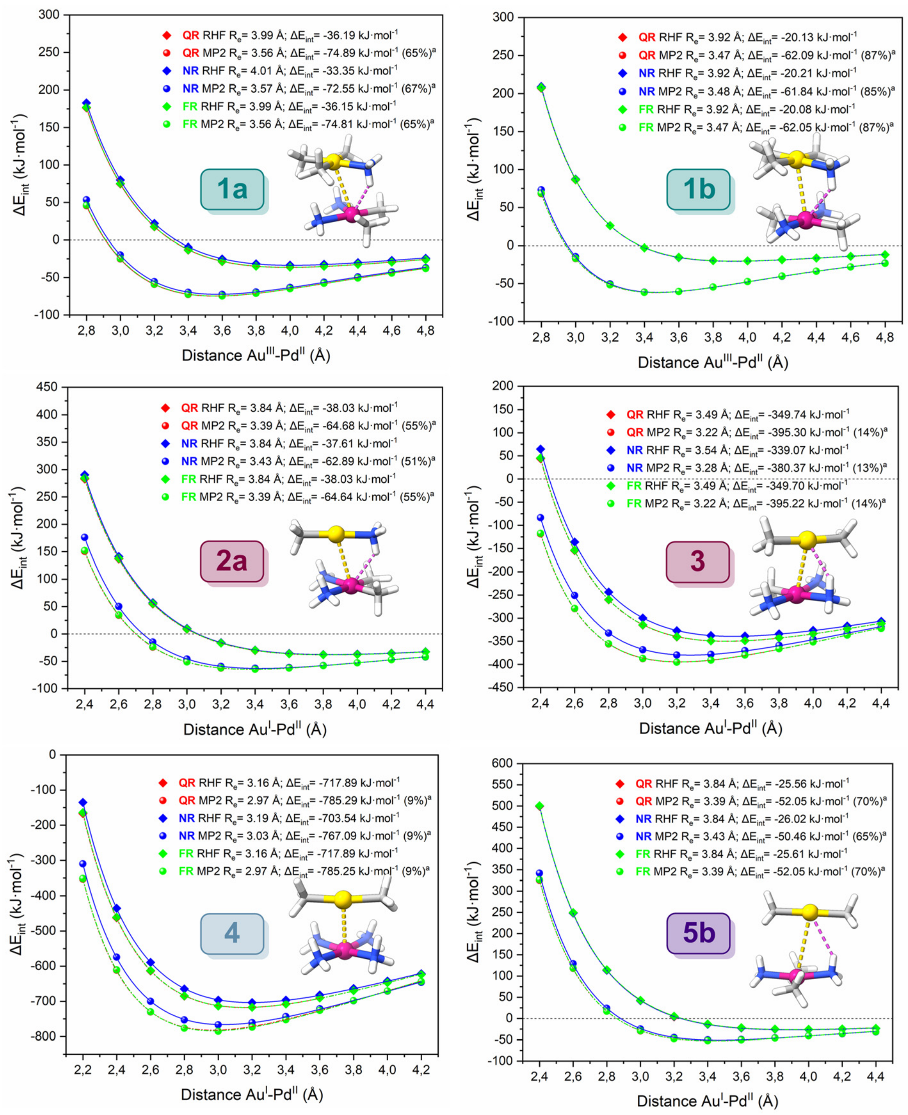

Fig. 3 Potential energy curves (PECs) of the total interaction energy as a function of the Au–Pd distance computed at the RHF/def2-TZVP and MP2/def2-TZVP levels of theory. Calculations were performed using quasi-relativistic (QR), nonrelativistic (NR), and fully relativistic (FR) ECPs. Raw data are included in the SI (Tables S4–S9). [a] Electron correlation contribution was quantified according to eqn (S3).

weakening compared to that calculated at the MP2 level of theory. For most models, electron correlation effects account for most of the overall stabilization, contributing approximately 55–88%, underscoring the dispersive character of these interactions. In contrast, models **3** and **4** exhibit a much smaller contribution, only 10–15%, which can be attributed to the dominant coulombic forces arising from the ionic nature of the fragments, in agreement with the previous discussion. The relative order of interaction strength among the models follows the sequence **4** ≫ **3** ≫ **1a** > **2a** ≈ **1b** ≈ **5b**. Interestingly, although the electron correlation contribution is slightly smaller than in analogous Au⋯Pt models,[68] the Au⋯Pd contact remains comparable, likely due to its more pronounced ionic character.

Given the well-established importance of relativistic effects in metallophilic interactions, we next evaluated their influence by comparing PECs computed with different ECP schemes (FR *vs.* NR; eqn (S4)). Overall, relativistic effects account for only 1–4% of the total interaction energy, significantly smaller than those reported for Au(I)⋯Au(I) and Au(I)⋯Hg(II) contacts (22–27%),[12,27] and even below those estimated for weaker interactions such as Au(III)⋯Au(III), Au(I)⋯Pt(II), or Au(I)⋯Ir(I) (2–15%).[67–69] This reduced impact is expected given that Pd is considerably lighter than those heavier congeners.[108] Strikingly, the interaction energy values at the PEC minima of the Au⋯Pd models are comparable to those of their Au⋯Pt analogues,[68] despite the markedly lower relativistic contribution. This observation further emphasizes the discrepancies in the influence of relativistic effects along a late transition metal group.[16]

Calculations employing NR-ECPs systematically lead to longer equilibrium distances and weaker interactions relative to QR- and FR-ECPs. In contrast, QR- and FR-ECPs yield virtually identical Au⋯Pd interaction energy values and Au–Pd distances. Given the negligible differences between FR- and QR-ECPs and the latter being the default implementation in the Gaussian 16 program, we adopted QR-ECPs for all subsequent calculations.

To more rigorously evaluate the interaction energy values, single-point counterpoise-corrected calculations were performed at the MP2-PECs minima using QR-ECPs, enabling direct comparison of MP2 with higher-level methods, SCS-MP2 and DLPNO-CCSD(T), which provide a more accurate description of electron correlation, as summarized in Table 1.

The results show that the MP2 level of theory agrees well with the more accurate SCS-MP2 and DLPNO-CCSD(T) methods. In fact, interaction energy values differ by only ≈0.4–10 kJ mol^{-1}, which seems an acceptable deviation. Interestingly, for some models, SCS-MP2 and DLPNO-CCSD(T) yield slightly stronger interaction energy values than MP2 ($\Delta E_{MP2} < 0$), which is unexpected since the MP2 level of theory typically exaggerates these interactions,[1,11–13] whereas the former methods generally provide more reliable descriptions. A similar trend was also observed for the Au⋯Pt interactions.[68]

To further clarify the role of Au⋯Pd interactions in dyad stabilization, we developed a decomposition scheme for our models to extract the metal–metal contribution ($\Delta E_{Au\text{–}Pd}$) from the total interaction energy (see Scheme S1 in the SI). Similar strategies have been successfully employed in previous studies.[20,67,111,112] For neutral models **1–2** and the anionic model **5b**, the Au⋯Pd interactions contribute 36% to 23% of the total interaction energy at the SCS-MP2 method and 33% to 18% at the DLPNO-CCSD(T) level of theory. Metallophilic interactions therefore stand out as a crucial component of dyad stabilization. Moreover, for models **3** and **4**, the Au⋯Pd component accounts for approximately 90% of the total interaction energy, reflecting a dominant electrostatic contribution largely localized on the metal centers, consistent with the PECs analysis. Nevertheless, while conceptually useful, this manual fragmentation remains approximate; thus, the extracted metal–metal contribution should be regarded as qualitative.

Considering these findings, the MP2 level of theory was deemed suitable for describing metallophilic interactions in these models, as it provides results consistent with higher-level methods. Thus, all subsequent computational analyses were carried out using the geometry located at the MP2 (QR-ECPs) minimum on the PEC of each model.

3.3 Electronic and bonding descriptors

Motivated by the presence of attractive noncovalent interactions in our computational models, we sought to evaluate a series of electronic and bonding descriptors to gain deeper insights into the nature and strength of Au⋯Pd interactions. The computed results are summarized in Table 2.

The NBO charge distribution reveals ligand-to-metal donation across all systems: the charge on Au(III) decreases to approximately +0.8, on Au(I) to +0.2–0.3, and on Pd(II) to +0.1–0.5. This redistribution mitigates electrostatic repulsion between the fragments, indicating that electron-donor ligands may support metallophilic interactions. For models **1a** and **1b**, which feature Au(III)⋯Pd(II) interactions, the palladium center loses electron density while the gold center gains it upon dimerization, consistent with a weak Pd → Au donor–acceptor interaction. In contrast, the Au(I)⋯Pd(II) models exhibit the opposite behaviour: Au(I) loses electron density whereas Pd(II) gains it upon dimerization, indicating a modest Au → Pd donation. This charge-transfer pattern aligns with the minor covalent contribution revealed by complementary analyses (*vide infra*).

To better characterize the strength of the metallophilic interactions, we evaluated the Wiberg bond order (WBO), intrinsic bond strength index (IBSI), and fuzzy bond order (FBO), each providing a complementary perspective on electron sharing and delocalization between the metal centers. All bond orders follow the relative trend: **4** ≫ **3** > **2a** > **5b** > **1b** > **1a**, reflecting the intrinsic strength of the Au⋯Pd interactions across the models. Interestingly, this ranking differs from the trends observed in the total interaction energies, highlighting that models **1b** and **1a** exhibit the weakest metallophilic interactions, yet their total interaction energy

Table 1 The counterpoise corrected interaction energy values (in kJ mol^{-1}) calculated at the SCS-MP2 and DLPNO-CCSD(T) levels of theory with the def2-TZVP basis sets, at the MP2 minimum of the PECs (R_e in Å)

Model	Method	R_e (Au–Pd)	ΔE_{int}	$\Delta E_{Au\text{–}Pd}$ [a]	ΔE_{MP2} [b]
1a	SCS-MP2	3.56	−80.37	−21.52 (27%)	−5.48
	DLPNO-CCSD(T)		−80.33	−18.43 (23%)	−5.44
1b	SCS-MP2	3.47	−65.50	−14.74 (23%)	−3.41
	DLPNO-CCSD(T)		−64.25	−11.48 (18%)	−2.16
2a	SCS-MP2	3.39	−67.21	−24.03 (36%)	−2.53
	DLPNO-CCSD(T)		−64.25	−21.24 (33%)	+0.43
3	SCS-MP2	3.22	−392.30	−355.03 (91%)	+3.00
	DLPNO-CCSD(T)		−390.93	−352.41 (90%)	+4.37
4	SCS-MP2	2.97	−780.51	−730.09 (94%)	+4.78
	DLPNO-CCSD(T)		−775.12	−722.34 (93%)	+10.17
5b	SCS-MP2	3.39	−52.01	−15.62 (30%)	+0.04
	DLPNO-CCSD(T)		−50.26	−12.81 (25%)	+1.79

[a] Au⋯Pd interaction energy values calculated from Scheme S1; raw data are listed in Tables S10 and S11; percentages within parentheses indicate their contribution to the total energy. [b] ΔE_{MP2} represents the energy difference with respect to the MP2/def2-TZVP level of theory (in kJ mol^{-1}).

Table 2 Effective charges of the metal centers and bond and interpenetration indices for the Au⋯Pd interactions. The charges of the atoms in their respective monomers are shown in parentheses

Model	Au q_{NBO} [a]	Pd q_{NBO} [a]	WBO[a]	IBSI[a]	IBSI[b]	FBO[a]	FBO[b]	$p_{\mathrm{Au-Pd}}$
1a	+0.79 (+0.82)	+0.10 (+0.09)	0.058	0.014	0.010	0.131	0.099	50.5
1b	+0.80 (+0.82)	+0.15 (+0.15)	0.063	0.016	0.012	0.177	0.138	56.0
2a	+0.26 (+0.23)	+0.08 (+0.09)	0.091	0.020	0.016	0.231	0.193	60.8
3	+0.23 (+0.20)	+0.25 (+0.28)	0.123	0.026	0.021	0.326	0.288	71.2
4	+0.21 (+0.20)	+0.44 (+0.53)	0.268	0.051	0.043	0.829	0.478	86.4
5b	+0.23 (+0.20)	+0.17 (+0.15)	0.083	0.018	0.014	0.225	0.191	60.8

[a] Calculated at the MP2/def2-TZVP level of theory. [b] Calculated at the DLPNO-CCSD(T)/def2-TZVP level of theory.

remains relatively high due to a larger number of secondary interactions, specifically metal–H contacts and classical H-bonds.

In line with these observations, most models show low bond order values, much closer to 0 than 1, consistent with predominantly noncovalent interactions. Model **4**, however, displays a markedly higher WBO value of 0.27, indicating that although the interaction remains fundamentally noncovalent, it incorporates a modest electron sharing contribution. Among the different bond order values, FBO values are consistently the highest, further indicating a small but detectable covalent component that increases the strength of the Au⋯Pd interaction. Notably, MP2 yields systematically larger bond orders than DLPNO-CCSD(T), with FBO values roughly twice as high, consistent with its well-known tendency to overestimate metallophilic interactions.

Finally, the recently proposed interpenetration index (p_{AB}) was computed to assess the extent of van der Waals shell overlapping between the gold and palladium atoms.[113] The typical distribution of aurophilic interactions ranges from 40 to 80%, with a maximum around 68%. Accordingly, the $p_{\mathrm{Au-Pd}}$ values in our models span 40–86%, in good agreement with these values. Moreover, the $p_{\mathrm{Au-Pd}}$ parameters follow the same trend observed in the bond order analysis, indicating that a higher percentage of van der Waals shell overlap corresponds to stronger Au⋯Pd interactions.

3.4 Interaction energy decomposition

In the next step, we dissected the interaction energy into its fundamental physical components, revealing the key forces that drive the stabilization of these Au–Pd systems. To this end, EDA-NOCV analysis was performed at the DLPNO-MP2 level of theory. This method decomposes the intrinsic interaction energy (ΔE_{int}) between two fragments of a molecule into physically meaningful contributions: electrostatics ($\Delta E_{\mathrm{elstat}}$), arising from the classical Coulomb forces; orbital term (ΔE_{orb}), which includes orbital mixing, charge transfer, induction and polarization; dispersion term (ΔE_{disp}), to consider the attractive forces associated with instantaneous electron density fluctuations; and Pauli repulsion ($\Delta E_{\mathrm{Pauli}}$), originating from the antisymmetrization of the wavefunctions imposed by the Pauli exclusion principle. Hence, the results are shown in Fig. 4, with raw data provided in Tables S12–S17 and additional theoretical background available in the SI.

The ΔE_{int} values of the overall interaction energy ($\Delta E^{\mathrm{total}}$) closely mirror the trends observed in the PEC analysis (see Fig. 3), showing excellent agreement with those results. Likewise, the isolated $\Delta E^{\mathrm{Au\cdots Pd}}$ component also follows the same pattern seen in the counterpoise-corrected interaction energies and in the bond order analyses (see Tables 1 and 2), validating the robustness of our decomposition strategy for disentangling the Au⋯Pd components of the overall interaction energy. In the following discussion, however, we move beyond absolute ΔE_{int} values to examine how each energy component contributes to shaping the overall interaction energy.

Inspection of the energy components of the $\Delta E^{\mathrm{total}}$ shown in Fig. 4 reveals that dispersion (ΔE_{disp}) is the dominant stabilizing term, contributing roughly 59–65% of the total interaction energy. Electrostatic forces ($\Delta E_{\mathrm{elstat}}$) represent the second major component (≈25–30%), while the orbital term (ΔE_{orb}) remains comparatively modest (≈10%). Taken together, these results show that the stabilization of these systems is governed primarily by dispersion-driven interactions. In contrast, models **3** and **4**, identified as ionic interactions in previous analyses, display a markedly different pattern: the electrostatic term dominates, contributing around 60% of the total stabilization. Even so, dispersion remains significant (30–35%), highlighting that although these models are primarily electrostatic in nature, dispersion provides substantial additional stabilization, making these interactions particularly strong.

Comparison with the $\Delta E^{\mathrm{Au\cdots Pd}}$ results confirms that all models exhibit attractive Au⋯Pd interactions. These results are noteworthy, as previous studies have suggested that metal–metal interactions of this type are intrinsically repulsive due to substantial M–M Pauli repulsion.[20,111,112] In our systems, the Au–Pd Pauli repulsion contribution is indeed large, representing about 13–37% of the total Pauli repulsion contribution, although it is effectively counterbalanced by the remaining attractive terms, yielding a net stabilizing interaction. Analysis of the individual $\Delta E^{\mathrm{Au\cdots Pd}}$ components shows that $\Delta E_{\mathrm{elstat}}$ increases across all models compared to $\Delta E^{\mathrm{total}}$, while ΔE_{orb} remains essentially unchanged. Although the dispersion contribution decreases, it remains the dominant stabilizing term in the non-ionic models, contributing to roughly 50% of the Au⋯Pd interaction. These findings underscore the fundamentally dispersive character of Au⋯Pd interactions and, more broadly, of the metallophilic contacts.

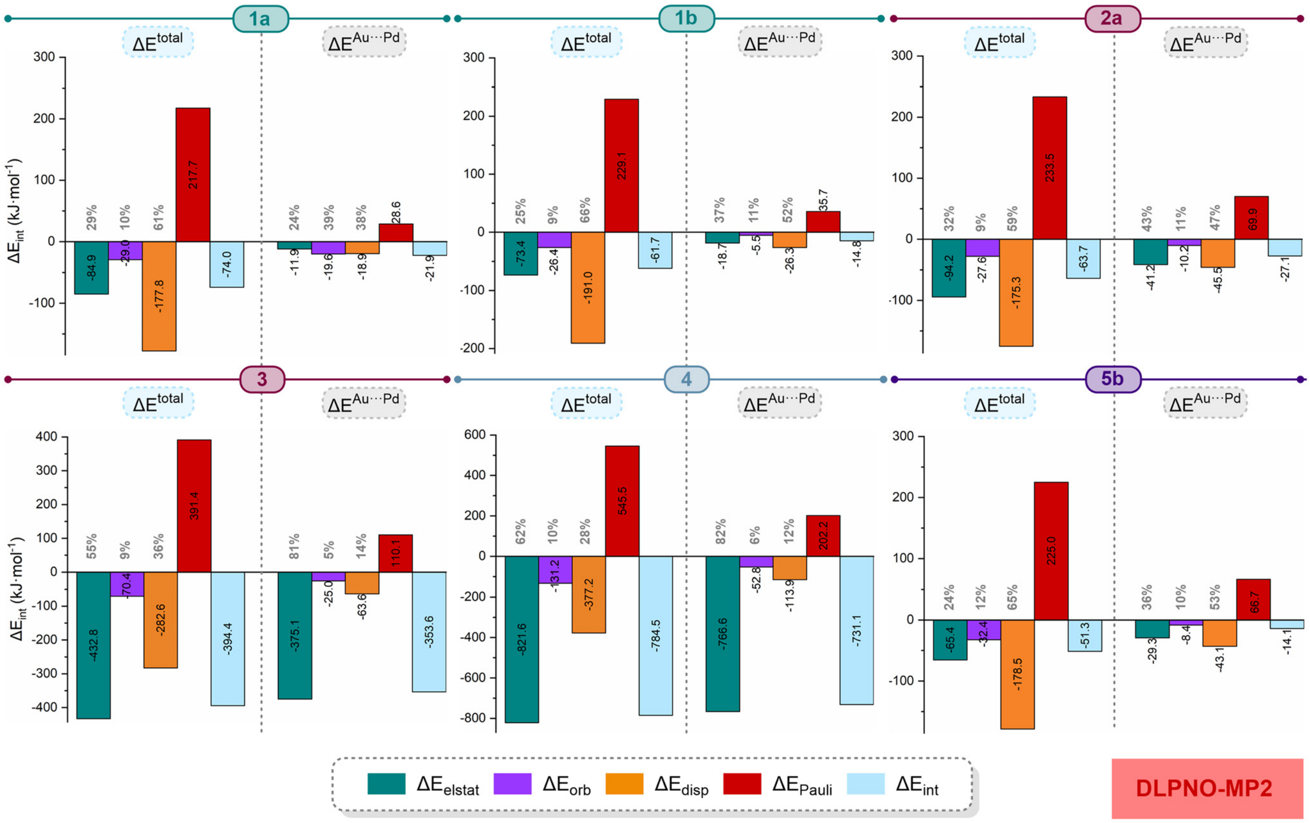

Fig. 4 EDA-NOCV contributions obtained at the DLPNO-MP2/def2-TZVP level of theory. Interaction energy values are given in kJ mol^{-1}, and percentage contributions are calculated relative to the total stabilizing energy, as defined in eqn (S7). The M–M component was determined following Scheme S1. Raw data are listed in Tables S12–17.

To complement this analysis, we also performed a local energy decomposition (LED) at the DLPNO-CCSD(T) framework, allowing us to pinpoint the ionic and dispersive forces that govern the stabilization of these models. Within this approach, the total interaction energy is partitioned into the Hartree–Fock term ($\Delta E_{\text{int}}^{\text{HF}}$), primarily associated with ionic contributions, and the electron correlation term ($\Delta E_{\text{int}}^{\text{C}}$). The latter is further decomposed into dispersive (ΔE_{disp}) and nondispersive ($\Delta E_{\text{no-disp}}$) terms. This methodology enables direct quantification of dispersion at the accurate DLPNO-CCSD(T) level of theory. The main results are listed in Table 3, with raw data provided in Table S18 and additional theoretical background available in the SI.

The interaction energy values closely follow the trends observed in the PECs and EDA-NOCV analyses, confirming the reliability of our computational protocol. Nevertheless, LED systematically overestimates these energy values compared to the values listed in Table 1, underscoring that counterpoise-corrected calculations provide a more accurate quantification.

Examining the LED components, it is evident that for most models, dispersion represents the dominant contribution, contributing to approximately 52% to 76% of the total interaction energy. In contrast, the remaining models **3** and **4** exhibit a much smaller dispersive contribution (around 10%), with the $\Delta E_{\text{int}}^{\text{HF}}$ term taking the lead, reflecting their predominantly ionic character. Across all models, the nondispersive correlation component, which partly accounts for the charge transfer and induction effects, plays only a minor role. These trends are fully consistent with the electron correlation contributions observed in the PECs analysis (see Fig. 3). Furthermore, comparison with the EDA-NOCV results (see Fig. 4) reveals a slightly larger ionic contribution and a comparable dispersion term, accompanied by a reduced orbital component. This trend suggests that the MP2 method modestly overestimates the covalent character within the total interaction energy.

To sum up, these analyses reveal that stabilization of these Au···Pd systems arises primarily from a balance of ionic and

Table 3 LED components of the total interaction energy (in kJ mol^{-1}) computed at the DLPNO-CCSD(T)/def2-TZVP level of theory[a]

Model	$\Delta E_{\text{int}}^{\text{HF}}$	ΔE_{disp} [b]	$\Delta E_{\text{no-disp}}$	ΔE_{int}
1a	−27.97	−51.13 (60%)	−5.84	−84.94
1b	−9.89	−52.61 (76%)	−7.09	−69.59
2a	−30.74	−38.86 (52%)	−4.44	−74.03
3	−342.97	−47.57 (12%)	−16.82	−407.36
4	−712.51	−55.69 (7%)	−26.06	−794.25
5b	−16.77	−37.88 (61%)	−7.07	−61.73

[a] LED components derived from Table S18 by applying eqn (S8)–(S13).
[b] Dispersion contribution (%) to ΔE_{int}.

dispersive forces, complemented by a subtle orbital (covalent) component. This highlights that metallophilic interactions do not originate from a single source but rather emerge from a delicate interplay of multiple contributions.

3.5 Topological analysis of the electron density

Finally, we mapped the electron density landscapes using QTAIM and IGMH topological analyses based on DLPNO-CCSD(T) and MP2 computed electron densities, offering a clear, intuitive and visual picture of the interactions shaping our computational models. Analyses of this type are seldom carried out at high-level correlated methods and are typically restricted to DFT, making their application in this work particularly valuable.

We first performed the QTAIM analysis, in which all (3, −1) bond critical points (BCPs) and their corresponding bond paths are as shown in Fig. S2. This approach provides a localized description of the electron density between two atoms, offering more detailed insights into bonding than the coarse measure of interaction energies. However, one should note that QTAIM parameters are not direct quantum-mechanical observables. In every model, a BCP is located along the Au⋯Pd bond path, confirming the presence of direct interaction between the two metal centers.[114,115] Additional BCPs associated with metal–H contacts or classical H-bonds were also identified. The QTAIM descriptors of the Au⋯Pd BCPs, obtained from DLPNO-CCSD(T) and MP2/def2-TZVP electron densities, are reported in Table 4 and Table S19, respectively, with further theoretical background provided in the SI.

The attractive nature of the Au⋯Pd interactions is clearly evidenced by the negative values of $\mathrm{sign}(\lambda_2)\cdot\rho_e(r)$ in the BCPs. Furthermore, the magnitude of electron density, $\rho_e(r)$, at the BCP correlates directly with the strength of the contact; the larger the $\rho_e(r)$, the stronger the interaction. Consequently, the relative strength among the models follows the trend **4** ≫ **3** ≫ **2a** ≈ **5b** > **1b** ≈ **1a**. These results indicate that Au(I)⋯Pd(II) interactions are markedly stronger than their Au(III)⋯Pd(II) counterparts, as expected, in excellent agreement with the bond parameters listed in Table 2 (*vide supra*).

When both the Laplacian of the electron density, $\nabla^2\rho_e(r)$, and the total energy density, $H(r)$, are considered, the nature of the interaction in the BCP can be classified more precisely.[116,117] Two clear trends emerge: (i) for the models exhibiting weaker Au⋯Pd interactions, namely, models **1a**, **1b**, and **5b**, the $\rho_e(r)$ values remain below 0.1 a.u., while both the Laplacian and $H(r)$ are positive. These features indicate a reduced electron density at the BCP, which is characteristic of closed-shell interactions of the van der Waals type; (ii) for models **4**, **3**, and **2a**, the same signs are observed except for $H(r)$, which becomes negative. The opposite signs of $\nabla^2\rho_e(r)$ and $H(r)$ suggest an interaction intermediate between purely ionic and covalent, implying that these Au⋯Pd contacts exhibit partial electron-sharing character. Accordingly, these topological parameters place these interactions at the borderline between weak noncovalent contacts and conventional hydrogen bonds, consistent with the view that metallophilic interactions are comparable in strength to H-bonds.[10]

The MP2 values are systematically larger than those obtained using the DLPNO-CCSD(T) method, reflecting the well-known tendency of the MP2 level to overestimate dispersive contributions. At this level of theory, all models exhibit opposite signs for $\nabla^2\rho_e(r)$ and $H(r)$, suggesting that MP2 also enhances the apparent covalent character of the metallophilic interactions. In line with this behavior, the larger contribution of the potential energy density, $V(r)$, at the MP2 level denotes a local charge concentration typical of shared-shell interactions. Conversely, in the DLPNO-CCSD(T) framework, the Lagrangian kinetic energy density, $G(r)$, prevails, indicating charge depletion consistent with closed-shell interactions.

Examining the $|V(r)|/G(r)$ ratio provides a sharper classification of the interactions.[118] At DLPNO-CCSD(T) electron density, models **4**, **3**, and **2a** (those with the strongest Au⋯Pd contacts) display ratios close to **1**, indicative of regular closed-shell interactions with a detectable degree of covalent character, in line with the other QTAIM descriptors. For the remaining models, the ratio falls slightly below **1**, consistent with closed-shell-type interactions. In contrast, the MP2 electron densities yield parameters fully characteristic of a regular closed-shell regime. Furthermore, the $G(r)/\rho_e(r)$ ratios point to metallic-type interactions and reveal that the donor–acceptor character increases in parallel with the growing covalency across the series.[119] Overall, the Au⋯Pd contacts remain essen-

Table 4 QTAIM descriptors of (3, −1) bond critical points (BCPs) between gold and palladium atoms calculated with the DLPNO-CCSD(T)/def2-TZVP electron density[a]

Model	$r_{\mathrm{Au–Pd}}$	$\mathrm{sign}(\lambda_2)\cdot\rho_e(r)$	$\nabla^2\rho_e(r)$	$H(r)\cdot10^3$	$G(r)$	$V(r)$	$\lvert V(r)\rvert/G(r)$	$G(r)/\rho_e$	E_{int} [b]	E_{int} [c]
1a	3.559	−0.0093	+0.0274	+0.4413	0.0064	−0.0060	0.9312	0.6863	7.84	7.22
1b	3.467	−0.0107	+0.0320	+0.4050	0.0076	−0.0072	0.9467	0.7138	9.45	8.57
2a	3.385	−0.0133	+0.0363	−0.1451	0.0092	−0.0094	1.0157	0.6928	12.30	10.39
3	3.219	−0.0180	+0.0497	−0.9741	0.0134	−0.0144	1.0726	0.7437	18.88	15.10
4	2.969	−0.0290	+0.0847	−3.2373	0.0244	−0.0277	1.1326	0.8419	36.30	27.50
5b	3.439	−0.0117	+0.0328	+0.1729	0.0080	−0.0079	0.9785	0.6897	10.32	9.05

[a] Distance Au–Pd ($r_{\mathrm{Au–Pd}}$ in Å), product of the sign of the second largest eigenvalue of the Hessian matrix of electron density ($\mathrm{sign}(\lambda_2)\cdot\rho_e(r)$ in a.u.), Laplacian of electron density ($\nabla^2\rho_e(r)$ in a.u.), electron energy density ($H(r)$ in a.u.), Lagrangian kinetic energy density ($G(r)$ in a.u.), potential energy density ($V(r)$ in a.u.), ratio $|V(r)|/G(r)$, ratio $G(r)|/\rho_e$ in a.u., and estimated interaction energies (E_{int} in kJ mol^{-1}). [b] Espinosa: $E_{\mathrm{int}} = -V(r)/2$. [c] Vener: $E_{\mathrm{int}} = 0.429G(r)$.

tially noncovalent, although increasing interaction strength is accompanied by a modest but discernible increase in covalent character.

Finally, the interaction energy values at the Au⋯Pd BCPs were estimated through the Espinosa and Vener approaches.[120,121] At the DLPNO-CCSD(T) level of electron density, the computed ΔE_{int} values range from 8 to 36 kJ mol^{-1} (Espinosa) and from 7 to 28 kJ mol^{-1} (Vener). At the MP2 level of theory, the values are slightly larger, spanning 9–39 kJ mol^{-1} (Espinosa) and 8–28 kJ mol^{-1} (Vener). Therefore, these values are significant, particularly for the models with a larger electrostatic component, which further supports the presence of the Au⋯Pd interaction.

Interestingly, although these interactions are weaker than classic Au(I)⋯Au(I) or Au(I)⋯Hg(II) contacts,[27,122] they rival those observed for Au(III)⋯ Au(III)[67] and even Au⋯Pt(II)[68] interactions. This strength suggests that the diminished relativistic contribution may be compensated by a more substantial electrostatic component. Moreover, it is important to note that these results are based on gas-phase calculations, so in the solid state, crystal packing and environmental effects could reinforce the interaction strength, while in solution, screening of the electrostatic component might weaken or even disrupt it.

Based on the QTAIM results, we next computed the IGMH isosurfaces along with their corresponding quantitative descriptors. This approach provides a powerful tool to visualize and analyze noncovalent interactions. Compared to the widely used NCI method,[123] IGMH offers several advantages, including multiple quantitative indices and clearer, more interpretable interaction isosurfaces.[124] Accordingly, the mapped IGMH isosurfaces and the most relevant quantitative parameters derived from the DLPNO-CCSD(T) and MP2 electron densities are presented in Fig. 5 and Fig. S3, respectively. Additional descriptors are listed in Tables S20–S33, and further theoretical details are provided in the SI.

Across all model systems, pronounced greenish-bluish regions emerge between the metal centers, signaling electron-rich zones ($\rho_e(r) > 0$) with an attractive character ($\lambda_2 < 0$). Combined with the presence of bond critical points and their connecting bond paths (Fig. S2), this offers compelling topological evidence for a genuine attractive interaction between gold and palladium atoms.

The IGMH indices provide a quantitative picture of the strength of Au(I)⋯Pd(II) interactions. The atomic pair index (δG^{pair}) gauges the contribution of each atom pair, while the atomic index (δG^{atom}) evaluates the role of individual atoms (see Tables S20 and S21). The intrinsic bond strength index for weak interactions (IBSIW) further differentiates their relative strength. In all cases, larger values denote stronger interactions. Consistently, δG^{pair} and IBSIW confirm the relative strength order of the Au⋯Pd contacts across the models, in line with bond orders and QTAIM analyses (*vide supra*). Moreover, δG^{atom} highlights the dominant role of the gold center in stabilizing the overall interaction, contributing ≈20–40%, whereas palladium contributes ≈20–25%. For the MP2 level of theory (see Fig. S3), the IGMH indices are systematically higher than those obtained using the DLPNO-CCSD(T) method, reflecting the trends observed throughout this work.

Alongside the metallophilic interactions, several additional secondary contacts are visible on the greenish and even bluish

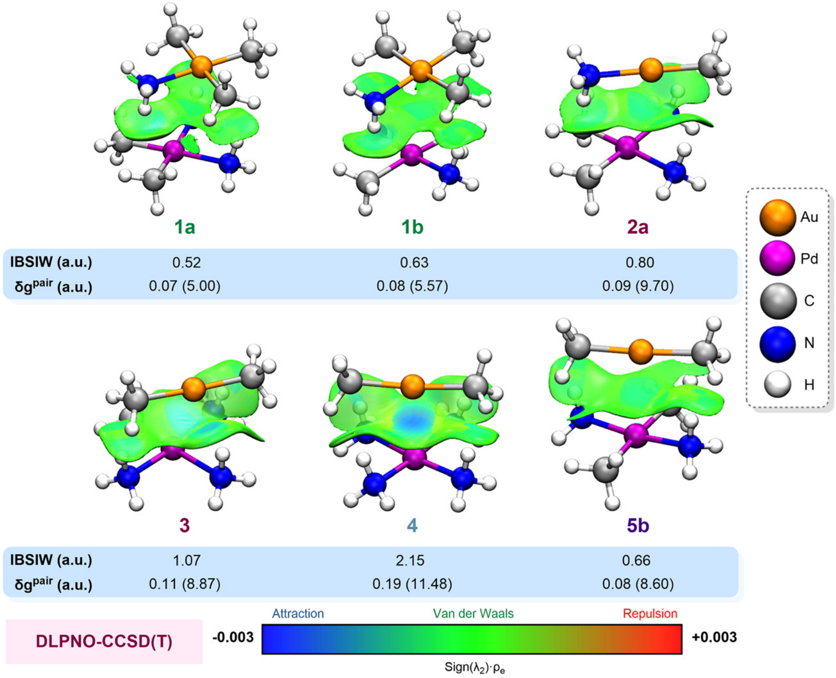

	1a	1b	2a
IBSIW (a.u.)	0.52	0.63	0.80
δg^{pair} (a.u.)	0.07 (5.00)	0.08 (5.57)	0.09 (9.70)

	3	4	5b
IBSIW (a.u.)	1.07	2.15	0.66
δg^{pair} (a.u.)	0.11 (8.87)	0.19 (11.48)	0.08 (8.60)

Fig. 5 IGMH map representations of the DLPNO-CCSD(T)/def2-TZVP electron density for models **1–5**. The isosurface maps correspond to an isovalue of δg^{inter} = 0.003 a.u. and are colored according to the BGR color scale, with a range from −0.003 to +0.003 a.u.

isosurfaces, showing their significant contribution to the overall stabilization. These interactions primarily involve metal–H bonding, a structural motif that has attracted considerable attention in contemporary chemical research.[38,41] To allow direct comparison with the Au⋯Pd interactions, Tables S22–S33 report the IGMH indices calculated for the BCPs of these interactions (see Fig. S2). Across all models, the Au⋯Pd interactions remain the key drivers of overall stabilization. Although, in models **1a** and **1b**, Pd(II)⋯H–N contacts rival its strength; in contrast, in models **2a** and **3**, Au(I)⋯H–N interactions play a similar role. These secondary contacts not only bolster the metallophilic interactions but, as revealed in the optimized structures (Fig. 1 and 2), can even compete with and occasionally masking them.

4. Conclusions

In summary, high-level computational calculations of unsupported models, derived from experimental Au(I)/Au(III) and Pd(II) complexes, reveal that the Au⋯Pd interactions exhibit the hallmarks of regular closed-shell interactions, governed predominantly by dispersion and electrostatic forces, with a minor, but perceptible, covalent component. Their attractive nature ultimately reflects a delicate interplay among dispersion, electrostatics, and covalent effects, whose relative contribution remains strongly system-dependent.

The multifaceted correlated computational protocol that we performed shows excellent consistency, demonstrating that electron correlation effects, mainly dispersion, are essential for accurately describing these interactions. Topological analyses further confirm their noncovalent and dispersive character, revealing bond critical points (BCPs) along the Au⋯Pd bond paths in the models, thus providing compelling evidence for attractive interactions between the metals. Moreover, metal–hydrogen bonding reinforces the metallophilic contacts and, in some cases, competes with them, displaying comparable interaction strengths.

The computed DLPNO-CCSD(T) interaction energy values (*ca.* 10–35 kJ mol^{-1}) are somewhat weaker than those typically reported for Au(I)⋯Au(I) or Au(I)⋯Hg(II) interactions (*ca.* 20–50 kJ mol^{-1}). Interestingly, their magnitude is comparable to those of Au(I)⋯Pt(II) or Au(III)⋯Au(III) contacts, which is unexpected given that palladium exhibits significantly weaker relativistic effects than platinum or gold. The PECs further corroborate the lower relativistic contribution of Pd, suggesting that factors beyond relativity, such as dispersion and electrostatic forces, play a more decisive role in stabilizing the Au⋯Pd interaction.

In view of our results, $[Pd(CH_3)(NH_3)_3][Au(CH_3)_2]$ (model **3**) and, especially, $\{[Pd(NH_3)_4][Au(CH_3)_2]\}^+$ (model **4**) emerge as the most promising candidates for achieving complexes featuring this type of interaction, primarily due to their strong electrostatic attraction. Consequently, ionic systems combining electron-donor ligands on gold with chelating N-donor ligands on palladium, are proposed as synthetically accessible platforms to enable the rational engineering of unsupported Au⋯Pd contacts. Ideally, these systems should feature planar, aromatic architectures capable of engaging in secondary interactions such as π-stacking or hydrogen bonding.

This work corroborated a strong consistency among diverse quantum chemical and topological analyses in describing metallophilic interactions, establishing a robust and transferable multifaceted correlated protocol for their accurate characterization. The computational results validate the reliability of these methodologies and underscore the pivotal role of quantum chemical modeling in the rational design of heterometallic complexes. Notably, the synthesis of related unsupported Au⋯Pd complexes is currently underway, aiming to experimentally validate the predicted interactions and further explore their structural and electronic properties.

Author contributions

F. R., J. M. L. and M. M.: conceptualization; F. R.: methodology; F. R.: formal analysis; F. R.: investigation, F. R.: visualization; M. E. O., J. M. L. and M. M.: supervision; F. R.: writing – original draft; F. R., M. E. O., J. M. L. and M. M.: writing – review & editing; M. E. O., J. M. L. and M. M.: funding acquisition; M. E. O., J. M. L. and M. M.: project administration. All authors contributed to manuscript preparation and revision and approved the final version.

Conflicts of interest

The authors declare no conflicts of interest.

Data availability

Supporting data are available within the article and its supplementary information (SI): additional computational details, theoretical background, optimized structures, PEC calculations, EDA-NOCV, LED, QTAIM, and IGMH analyses, Cartesian coordinates of the optimized geometries for models **1–5** and additional references (PDF). See DOI: https://doi.org/10.1039/d6dt00023a.

Acknowledgements

We gratefully acknowledge financial support from the DGI MCINN/FEDER project number PID2022-139739NB-I00 (AEI/FEDER, UE) and from “ERDF A way of making Europe”. Computational resources were provided by the Beronia cluster at the Universidad de La Rioja, supported by the MINECO/FEDER grant number UNLR-094-2C-225. We also thank Dr. Raúl Losantos for valuable discussions regarding the ORCA calculations.

References

1 P. Pyykkö, *Chem. Rev.*, 1997, **97**, 597.

2 P. Pyykkö, *Angew. Chem., Int. Ed.*, 2004, **43**, 4412.

3 A. Laguna, *Modern Supramolecular Gold Chemistry*, Wiley-VCH, Weinheim, 2008.

4 C. Silvestru and A. Laguna, *The Chemistry of Organogold Compounds*, Wiley VCH, Weinheim, 2015, vol. 2, p. 409.

5 K. M. C. Wong, V. K. M. Au and V.-W. W. Yam, *Comprehensive Inorganic Chemistry II*, Elsevier, 2013, vol. 8, p. 59.

6 T. P. Seifert, V. R. Naina, T. J. Feuerstein, N. D. Knöfel and P. W. Roesky, *Nanoscale*, 2020, **12**, 20065.

7 S. Sculfort and P. Braunstein, *Chem. Soc. Rev.*, 2011, **40**, 2741.

8 F. Scherbaum, A. Grohmann, B. Huber, C. Krüger and H. Schmidbaur, *Angew. Chem., Int. Ed. Engl.*, 1988, **27**, 1544.

9 P. Pyykkö, J. Li and N. Runeberg, *Chem. Phys. Lett.*, 1994, **218**, 133.

10 Q. Zheng, S. Borsley, G. S. Nichol, F. Duarte and S. L. Cockroft, *Angew. Chem., Int. Ed.*, 2019, **58**, 12617.

11 P. Pyykkö, N. Runeberg and F. Mendizabal, *Chem. – Eur. J.*, 1997, **3**, 1451.

12 F. Mendizabal and P. Pyykkö, *Phys. Chem. Chem. Phys.*, 2004, **6**, 900.

13 P. Pyykkö, *Chem. Soc. Rev.*, 2008, **37**, 1967.

14 Y. Jiang, S. Álvarez and R. Hoffmann, *Inorg. Chem.*, 1985, **24**, 749.

15 P. Pyykkö and Y. Zhao, *Angew. Chem., Int. Ed. Engl.*, 1991, **30**, 604.

16 E. O'Grady and N. Kaltsoyannis, *Phys. Chem. Chem. Phys.*, 2004, **6**, 680.

17 S. Grimme and J.-P. Djukic, *Inorg. Chem.*, 2011, **50**, 2619.

18 M. B. Brands, J. Nitsch and C. Fonseca-Guerra, *Inorg. Chem.*, 2018, **57**, 2603.

19 E. Andris, P. C. Andrikopoulos, J. Schulz, J. Turek, A. Růžička, J. Roithová and L. Rulíšek, *J. Am. Chem. Soc.*, 2018, **140**, 2316.

20 Q. Wan, J. Yang, W.-P. To and C.-M. Che, *Proc. Natl. Acad. Sci. U. S. A.*, 2020, **118**, e2019265118.

21 F. Reboiro, M. E. Olmos, J. M. López-de-Luzuriaga and M. Monge, *Dalton Trans.*, 2026, **55**, 1024.

22 H. Schmidbaur and A. Schier, *Chem. Soc. Rev.*, 2012, **41**, 370.

23 H. Schmidbaur and A. Schier, *Angew. Chem., Int. Ed.*, 2014, **54**, 746.

24 N. V. S. Harisomayajula, S. Makovetskyi and Y.-C. Tsai, *Chem. – Eur. J.*, 2019, **25**, 8936.

25 H. Schmidbaur and A. Schier, *Organometallics*, 2015, **34**, 2048.

26 R. Donamaría, V. Lippolis, J. M. López-de-Luzuriaga, M. Monge, M. Nieddu and M. E. Olmos, *Inorg. Chem.*, 2018, **57**, 11099.

27 J. M. López-de-Luzuriaga, M. Monge, M. E. Olmos, D. Pascual and T. Lasanta, *Chem. Commun.*, 2011, **47**, 6795.

28 T. E. Karpiuk, S. Mahato, T. Storr and D. B. Leznoff, *Chem. Commun.*, 2024, **60**, 3914.

29 X. Yin, S. A. Warren, Y. T. Pan, K. C. Tsao, D. L. Gray, J. Bertke and H. Yang, *Angew. Chem., Int. Ed.*, 2014, **53**, 14087.

30 Q. Wan, W. P. To, C. Yang and C.-M. Che, *Angew. Chem., Int. Ed.*, 2018, **57**, 3089.

31 X. Zheng, M. H.-Y. Chan, A. K.-W. Chan, S. Cao, M. Ng, F. K. Sheong, C. Li, E. C. Goonetilleke, W. W. Y. Lam, T.-C. Lau, X. Huang and V. W.-W. Yam, *Proc. Natl. Acad. Sci. U. S. A.*, 2022, **119**, e2116543119.

32 S. Raju, H. B. Singh and R. J. Butcher, *Dalton Trans.*, 2020, **49**, 9099.

33 R. Donamaría, J. M. López-de-Luzuriaga, M. Monge and M. E. Olmos, *Chem. Sci.*, 2015, **6**, 2022.

34 J. M. López-de-Luzuriaga, M. Monge, M. E. Olmos, M. Rodríguez-Castillo and A. Sorroche, *Phys. Chem. Chem. Phys.*, 2021, **23**, 10174.

35 D. Royo, S. Moreno, M. Rodríguez-Castillo, M. Monge, M. E. Olmos, F. I. Zubkov, A. A. Pronina, G. Mahmoudi and J. M. López-de-Luzuriaga, *Dalton Trans.*, 2024, **53**, 4652.

36 E. J. Fernández, A. Laguna, J. M. López-de-Luzuriaga, M. Monge, M. Nema, M. E. Olmos, J. Pérez and C. Silvestru, *Chem. Commun.*, 2007, 571.

37 E. R. T. Tiekink, *Coord. Chem. Rev.*, 2014, **275**, 130.

38 H. Schmidbaur, H. G. Raubenheimer and L. Dobrzańska, *Chem. Soc. Rev.*, 2014, **43**, 345.

39 D. M. Ivanov, N. A. Bokach, V. Yu. Kukushkin and A. Frontera, *Chem.–Eur. J.*, 2021, **28**, e202103173.

40 I. Benito, R. M. Gomila and A. Frontera, *CrystEngComm*, 2022, **24**, 4440.

41 A. Sorroche, F. Reboiro, M. Monge and J. M. López-de-Luzuriaga, *ChemPlusChem*, 2024, **89**, e202400273.

42 M. J. Katz, K. Sakaib and D. B. Leznoff, *Chem. Soc. Rev.*, 2008, **37**, 1884.

43 Q. Wan, J. Xia, W. Lu, J. Yang and C.-M. Che, *J. Am. Chem. Soc.*, 2019, **141**, 11572.

44 N. Mirzadeh, S. H. Privér, A. J. Blake, H. Schmidbaur and S. K. Bhargava, *Chem. Rev.*, 2020, **120**, 7551.

45 E. Tkatchouk, N. P. Mankad, D. Benitez, W. A. Goddard and F. D. Toste, *J. Am. Chem. Soc.*, 2011, **133**, 14293.

46 M. H. Larsen, K. N. Houk and A. S. K. Hashmi, *J. Am. Chem. Soc.*, 2015, **137**(33), 10668.

47 E. S. Smirnova and A. M. Echevarren, *Angew. Chem., Int. Ed.*, 2013, **52**, 9023.

48 M. C.-L. Yeung and V. W.-W. Yam, *Chem. Soc. Rev.*, 2015, **44**, 4192.

49 A. Lázaro, A. Pinto and L. Rodríguez, *Coord. Chem. Rev.*, 2026, 217411.

50 T. Seki, Y. Takamatsu and H. Ito, *J. Am. Chem. Soc.*, 2016, **138**, 6252.

51 T. Seki, N. Tokodai, S. Omagari, T. Nakanishi, Y. Hasegawa, T. Iwasa, T. Taketsugu and H. Ito, *J. Am. Chem. Soc.*, 2017, **139**, 6514.

52 S. Moreno, D. Royo, A. G. El Hachimi, M. Rodríguez-Castillo, M. Monge, M. E. Olmos and J. M. López-de-Luzuriaga, *Dalton Trans.*, 2023, **52**, 17119.

53 V. W.-W. Yam, V. K.-M. Au and S. Y.-L. Leung, *Chem. Rev.*, 2015, **115**, 7589.

54 M.-C. Tang, A. K.-W. Chan, M.-Y. Chan and V. W.-W. Yam, *Top. Curr. Chem.*, 2016, **374**, 46.

55 O. Crespo, A. Laguna, E. J. Fernández, J. M. López-de-Luzuriaga, P. G. Jones, M. Teichert, M. Monge, P. Pyykkö, N. Runeberg, M. Schütz and H.-J. Werner, *Inorg. Chem.*, 2000, **39**, 4786.

56 B.-H. Xia, H.-X. Zhang, C.-M. Che, K.-H. Leung, D. L. Phillips, N. Zhu and Z.-Y. Zhou, *J. Am. Chem. Soc.*, 2003, **125**, 10362.

57 A. Bondi, *J. Phys. Chem.*, 1964, **68**, 441.

58 S. S. Batsanov, *Inorg. Mater.*, 2001, **37**, 871.

59 S. A. Alvarez, *Dalton Trans.*, 2013, **42**, 8617.

60 E. Wächtler, S. H. Privér, J. Wagler, T. Heine, L. Zhechkov, M. A. Bennett and S. K. Bhargava, *Inorg. Chem.*, 2015, **54**, 6947.

61 P. Wu, X. Yu, L. Cheng and K. Wang, *J. Phys. Chem. A*, 2024, **128**, 6362.

62 M. Sircoglou, M. Mercy, N. Saffon, Y. Coppel, G. Bouhadir, L. Maron and D. Bourissou, *Angew. Chem., Int. Ed.*, 2009, **48**, 3454.

63 J. Bauer, H. Braunschweig and R. D. Dewhurst, *Chem. Rev.*, 2012, **112**, 4329.

64 P. Buchwalter, J. Rose and P. Braunstein, *Chem. Rev.*, 2015, **115**, 28.

65 J. Campos, *Nat. Rev. Chem.*, 2020, **4**, 696.

66 E. Serrano-Díez, A. Pita-Milleiro, J. Rangel-García, J. J. Moreno, M. Roselló-Merino and J. Campos, *J. Am. Chem. Soc.*, 2025, **147**, 1271.

67 D. Blasco, F. Reboiro, D. Sundholm, M. E. Olmos, M. Monge and J. M. López-de-Luzuriaga, *Dalton Trans.*, 2023, **52**, 2219.

68 F. Reboiro, D. Blasco, M. E. Olmos, M. Monge and J. M. López-de-Luzuriaga, *Inorg. Chem.*, 2025, **64**, 17121.

69 F. Reboiro, M. E. Olmos, M. Monge and J. M. López-de-Luzuriaga, *Inorg. Chem.*, 2025, **64**, 17569.

70 M. J. Frisch, G. W. Trucks, H. B. Schlegel, G. E. Scuseria, M. A. Robb, J. R. Cheeseman, G. Scalmani, V. Barone, G. A. Petersson, H. Nakatsuji, X. Li, M. Caricato, A. V. Marenich, J. Bloino, B. G. Janesko, R. Gomperts, B. Mennucci, H. P. Hratchian, J. V. Ortiz, A. F. Izmaylov, J. L. Sonnenberg, D. Williams-Young, F. Ding, F. Lipparini, F. Egidi, J. Goings, B. Peng, A. Petrone, T. Henderson, D. Ranasinghe, V. G. Zakrzewski, J. Gao, N. Rega, G. Zheng, W. Liang, M. Hada, M. Ehara, K. Toyota, R. Fukuda, J. Hasegawa, M. Ishida, T. Nakajima, Y. Honda, O. Kitao, H. Nakai, T. Vreven, K. Throssell, J. A. Montgomery Jr., J. E. Peralta, F. Ogliaro, M. J. Bearpark, J. J. Heyd, E. N. Brothers, K. N. Kudin, V. N. Staroverov, T. A. Keith, R. Kobayashi, J. Normand, K. Raghavachari, A. P. Rendell, J. C. Burant, S. S. Iyengar, J. Tomasi, M. Cossi, J. M. Millam, M. Klene, C. Adamo, R. Cammi, J. W. Ochterski, R. L. Martin, K. Morokuma, O. Farkas, J. B. Foresman and D. J. Fox, *Gaussian 16 Rev. C.01*, Wallingford CT, 2016.

71 C. C. J. Roothaan, *Rev. Mod. Phys.*, 1951, **23**, 69.

72 C. Møller and M. S. Plesset, *Phys. Rev.*, 1934, **46**, 618.

73 M. J. Frisch, M. Head-Gordon and J. A. Pople, *Chem. Phys. Lett.*, 1990, **166**, 275.

74 P. Hohenberg and W. Kohn, *Phys. Rev.*, 1964, **136**, B864.

75 W. Kohn and L. J. Sham, *Phys. Rev.*, 1965, **140**, A1133.

76 M. Ernzerhof and G. E. Scuseria, *J. Chem. Phys.*, 1999, **110**, 5029.

77 S. Grimme, J. Antony, S. Ehrlich and H. Krieg, *J. Chem. Phys.*, 2010, **132**, 154104.

78 Y. Zhao and D. G. Truhlar, *J. Chem. Phys.*, 2006, **125**, 194101.

79 Y. Zhao and D. G. Truhlar, *Theor. Chem. Acc.*, 2008, **120**, 215.

80 F. Weigend and R. Ahlrichs, *Phys. Chem. Chem. Phys.*, 2005, **7**, 3297.

81 D. Andrae, U. Häußermann, M. Dolg, H. Stoll and H. Preuß, *Theor. Chim. Acta*, 1990, **77**, 123.

82 M. Gerenkamp and S. Grimme, *Chem. Phys. Lett.*, 2004, **392**, 229.

83 E. van Lenthe, J. G. Snijders and E. J. Baerends, *J. Chem. Phys.*, 1996, **105**, 6505.

84 F. Neese, F. Wennmohs, U. Becke and C. Riplinger, *J. Chem. Phys.*, 2020, **152**, 224108.

85 B. Helmich-Paris, B. de Souza, F. Neese and R. Izsák, *J. Chem. Phys.*, 2021, **155**, 104109.

86 S. F. Boys and F. Bernardi, *Mol. Phys.*, 1970, **19**, 553.

87 D. R. Herschbach and V. W. Laurie, *J. Chem. Phys.*, 1961, **35**, 458.

88 P. Schwerdtfeger, M. Dolg, W. H. E. Schwarz, G. A. Bowmaker and P. D. W. Boyd, *J. Chem. Phys.*, 1989, **91**, 1762.

89 D. Figgen, G. Rauhut, M. Dolg and H. Stoll, *Chem. Phys.*, 2005, **311**, 227.

90 K. A. Peterson, D. Figgen, M. Dolg and H. Stoll, *J. Chem. Phys.*, 2007, **126**, 124101.

91 C. Riplinger and F. Neese, *J. Chem. Phys.*, 2013, **138**, 034106.

92 E. D. Glendening, C. R. Landis and F. Weinhold, *Wiley Interdiscip. Rev.: Comput. Mol. Sci.*, 2011, **2**, 1.

93 K. B. Wiberg, *Tetrahedron*, 1968, **24**, 1083.

94 J. Klein, H. Khartabil, J.-C. Boisson, J. Contreras-García, J.-P. Piquemal and E. Hénon, *J. Phys. Chem. A*, 2020, **124**, 1850.

95 I. Mayer and P. Salvador, *Chem. Phys. Lett.*, 2004, **383**, 368.

96 T. Lu and F. Chen, *J. Comput. Chem.*, 2012, **33**, 580.

97 T. Ziegler and A. Rauk, *Theor. Chim. Acta*, 1977, **46**, 1.

98 M. Mitoraj and A. Michalak, *J. Mol. Model.*, 2007, **13**, 347.

99 P. Pinski, C. Riplinger, E. F. Valeev and F. Neese, *J. Chem. Phys.*, 2015, **143**, 034108.

100 W. B. Schneider, G. Bistoni, M. Sparta, M. Saitow, C. Riplinger, A. A. Auer and F. Neese, *J. Chem. Theory Comput.*, 2016, **12**, 4778.

101 R. F. W. Bader, *Chem. Rev.*, 1991, **91**, 893.
102 T. Lu and Q. Chen, *J. Comput. Chem.*, 2022, **43**, 539.
103 W. Humphrey, A. Dalke and K. Schulten, *J. Mol. Graphics*, 1996, **14**, 3.
104 R. Kumar and C. Nevado, *Angew. Chem., Int. Ed.*, 2017, **56**, 1994.
105 R. P. Herrera and M. C. Gimeno, *Chem. Rev.*, 2021, **121**, 8311.
106 V. K. Jain, *Coord. Chem. Rev.*, 2021, **427**, 213546.
107 C. Puzzarini, *Int. J. Quantum Chem.*, 2016, **116**, 1513.
108 A. Das, U. Das and A. K. Das, *Coord. Chem. Rev.*, 2023, **479**, 215000.
109 X. Yu, T. Jin, K. Wang, D. Li and L. Cheng, *J. Chem. Phys.*, 2022, **156**, 104103.
110 A. N. Chernyshev, M. V. Chernysheva, P. Hirva, V. Y. Kukushkin and M. Haukka, *Dalton Trans.*, 2015, **44**, 14523.
111 S. Xu, Q. Wan, J. Yang and C.-M. Che, *J. Phys. Chem. Lett.*, 2024, **15**, 2193.
112 Y. Zhang and Q. Wan, *Inorg. Chem. Front.*, 2025, **12**, 6769.
113 S. Alvarez and J. Echeverría, *Chem. Sci.*, 2023, **14**, 11647.
114 R. F. W. Bader, *J. Phys. Chem. A*, 1998, **102**, 7314.
115 R. F. W. Bader, *J. Phys. Chem. A*, 2009, **113**, 10391.
116 R. Bianchi, G. Gervasio and D. Marabello, *Inorg. Chem.*, 2000, **39**, 2360.
117 S. Dinda and A. G. Samuelson, *Chem. – Eur. J.*, 2012, **18**, 3032.
118 W. Nakanishi and S. Hayashi, *J. Phys. Chem. A*, 2013, **117**, 1795.
119 P. Macchi, D. M. Proserpio and A. Sironi, *J. Am. Chem. Soc.*, 1998, **120**, 13429.
120 E. Espinosa, E. Molins and C. Lecomte, *Chem. Phys. Lett.*, 1998, **285**, 170.
121 M. V. Vener, A. N. Egorova, A. V. Churakov and V. G. Tsirelson, *J. Comput. Chem.*, 2012, **33**, 2303.
122 S. Burguera, A. Bauzá and A. Frontera, *Phys. Chem. Chem. Phys.*, 2024, **26**, 16550.
123 E. R. Johnson, S. Keinan, P. Mori-Sánchez, J. Contreras-García, A. J. Cohen and W. Yang, *J. Am. Chem. Soc.*, 2010, **132**, 6498.
124 T. Lu, *Angew. Chem., Int. Ed.*, 2025, **64**, e202504895.